

# Diurnal Asymmetry in the GERB SW Fluxes

Cédric Bertrand, Joanna Futyán, Alessandro Ipe, Luis Gonzalez, and Nicolas Clerbaux

**Abstract**—The launch of the Geostationary Earth Radiation Budget (GERB) instrument onboard the Meteorat 8 allows a diurnal sampling of the Earth's Radiation Budget for the first time, providing a unique and important addition to polar-orbiting measurements. However, preliminary data from the GERB instrument exhibit systematic asymmetry in the short-wave (SW) flux diurnal variation. Such asymmetries are not found in the Clouds and the Earth's Radiant Energy System angular distribution models used to convert the directional broad-band GERB SW radiances to fluxes. Comparison between angularly matched estimations of reflected SW flux at the top of the atmosphere from the Spinning Enhanced Visible and Infra Red Imager (SEVIRI) and GERB data indicates that the SEVIRI spectral modeling could be a major issue. In addition, the results indicate that other factors such as the GERB SW geolocation, the GERB detector spectral response functions, the GERB nominal footprint resolution, and cloud cover could also potentially have an influence on the diurnal evolution of the GERB SW fluxes, as they can erroneously impact on the GERB SW correction factor.

**Index Terms**—Remote sensing, satellites, solar energy, solar radiation.

## I. INTRODUCTION

**B**EGINNING in the mid-1960s, Earth-orbiting satellites began to play an important role in making measurements of the Earth's radiation flux (see, e.g., [11]). Raschke *et al.* [15] developed radiation budget maps using measurements from a scanning radiometer that had a number of relatively narrow-bands (NBs). Because of the intermittent operation of the instrument, it was necessary to accumulate a month of data in order to produce a map of albedo and outgoing long-wave (LW) radiation (OLR). A major accomplishment of the 1980s was the design, launch, and data processing of satellite-based moderate resolution broad-band (BB) fluxes in the Earth Radiation Budget Experiment (ERBE) [1]. However, it is known that ERBE observations have some fundamental flaws, including imprecise angular models used to convert directional radiances to fluxes, limited scene identification capabilities needed to accurately estimate cloud radiative forcing, and very limited diurnal sampling [19]. The Clouds and the Earth's Radiant Energy System (CERES) [20] experiment marked the beginning of a new generation of instruments and greatly improved radiation budget products. CERES instruments were launched aboard the TRMM in November

1997 and the EOS Terra and Aqua satellites in December 1999 and May 2002, respectively. CERES is designed to provide multiple view angles to allow for better transformation of radiances to fluxes and uses improved scene identification to aid in improved estimates of cloud radiative forcing. Although the processing of CERES data is coordinated with three-hourly geostationary satellite imaging data, the maximum of four observations per day does not allow the diurnal cycle to be fully resolved.

This latter problem is being approached with the Geostationary Earth Radiation Budget (GERB) [10] instrument aboard Meteorat-8 (hereinafter, "MS-8") together with the new Spinning Enhanced Visible and Infra Red Imager (SEVIRI) [17]. GERB is designed to exploit the geostationary orbit to make unique Earth radiation budget (ERB) measurements over Europe and Africa. The high time resolution possible from this orbit resolves the problem of diurnal sampling of the ERB and provides a unique and important addition to polar-orbiting measurements. However, preliminary data from the GERB instrument exhibit systematic asymmetry in the short-wave (SW) flux diurnal variation. Such asymmetries are not found in the angular distribution models (ADMs) built from a statistical analysis of nine months of CERES-TRMM measurements [13] (hereinafter, "CERES-TRMM ADMs") used to convert the directional BB GERB radiances to fluxes.

In this paper, we investigate the possible origin(s) of such asymmetries. This is done by analyzing both GERB and GERB-like fluxes (i.e., reflected SW flux values computed from SEVIRI data only). Before focusing on the flux asymmetry, we first start by briefly describing the method implemented at the Royal Meteorological Institute of Belgium (RMIB) to estimate the reflected SW GERB(-like) fluxes at the  $3 \times 3$  SEVIRI pixel resolution from the combined use of SEVIRI and GERB data.

## II. DERIVATION OF THE TOP-OF-ATMOSPHERE (TOA) REFLECTED GERB SW FLUX

When estimating the radiative fluxes at the TOA, the prime instrumental characteristics of importance are the spectral response functions and the radiometric calibrations of the channels, as any calibration error will propagate through the processing up to the final products.

### A. Instrument Characteristics

The SEVIRI instrument is a 12-channel imager that observes the full disk of the Earth with a repeat cycle of 15 min. SEVIRI has eight channels in the thermal infrared (IR) at 3.9, 6.2, 7.3, 8.7, 9.7, 10.8, 12.0, and 13.4  $\mu\text{m}$ , three channels in the solar at 0.6, 0.8, and 1.6  $\mu\text{m}$ , and a high-resolution visible (HRV) channel (about 0.4 to 1.1  $\mu\text{m}$ ). The SEVIRI spatial resolution is 4.8 km at nadir, except for the HRV channel, whose spatial resolution is 1.67 km at nadir. The thermal IR channels have

Manuscript received June 15, 2005; revised May 23, 2006. This work was supported by the Federal Office for Scientific, Technical and Cultural Affairs (Belgian State, Prime Minister's Office) under ProDEX Program (PRODEX-8).

C. Bertrand, A. Ipe, L. Gonzalez, and N. Clerbaux are with the Department of Observations, Section Remote Sensing from Space, Royal Meteorological Institute of Belgium, 1180 Brussels, Belgium (e-mail: Cedric.Bertrand@oma.be).

J. Futyán was with the Space and Atmospheric Physics, Imperial College, SW7 2AZ London, U.K. She is now with the Department of Applied Mathematics and Applied Physics and the Institute for Space Studies, Columbia University, New York, NY 10027 USA.

Digital Object Identifier 10.1109/TGRS.2006.881119

an onboard black body calibration with an accuracy better than 1 K. The solar channels are calibrated postlaunch with an operational vicarious procedure that incorporates stable desert targets and aims at an accuracy of 5% [18].

The GERB instrument is a visible-IR radiometer. It measures the SW radiance in the solar waveband from 0.32 to 4  $\mu\text{m}$  and the total radiance from 0.32 to 100  $\mu\text{m}$ . Knowledge of the GERB TOTAL and SW channel spectral response (the product of instrument throughput and detector responsivity) is required for converting the measured detector voltages into radiances for the TOTAL and SW channels. The measurements necessary to formulate this spectral response were made during the preflight ground calibration [14]. Data from the onboard black body source and solar diffuser (integrating sphere) allow the ground calibration of GERB to be continually reevaluated in flight. With a nominal pixel size of about 45 km by 40 km (north-south  $\times$  east-west) at nadir view, it obtains an absolute accuracy that is better than  $2.4 \text{ W} \cdot \text{m}^{-2} \cdot \text{sr}^{-1}$  ( $< 1\%$ ) in the SW [18]. The cycle time for the full disk is 5.38 min for both channels (16.55 min for full radiometric performance).

### B. Unfiltering

Accurate estimation of the unfiltered reflected solar radiances requires that the variations of the instrument sensitivity with wavelength are removed from the filtered directional SW radiance measurements  $L_{\text{SW}}^f$ . Unfiltered reflected SW radiance is defined as follows:

$$L_{\text{SW}}^{\text{uf}} = \int_0^{\infty} I_{\lambda}^r d\lambda \quad (1)$$

where  $\lambda$  (in microns) is the wavelength and  $I_{\lambda}^r$  (in watts per square meter per steradian per micron) represents the reflected spectral solar radiances. The unfiltered SW radiance is determined from the measured filtered SW radiance, which can be modeled as

$$L_{\text{SW}}^f = \int_0^{\infty} S_{\lambda}^{\text{SW}} I_{\lambda} d\lambda \quad (2)$$

where  $S_{\lambda}^{\text{SW}}$  is the SW spectral response function of the instrument ( $0 \leq S_{\lambda}^{\text{SW}} \leq 1.0$ ) and  $I_{\lambda}$  is the spectral radiance incident on the instrument. The averaged spectral response functions for the GERB detectors are shown in Fig. 1.

SEVIRI NB measurements are used to retrieve information about the spectral distribution of the observed radiation. The unfiltered radiances  $L^{\text{uf}}$  are estimated by multiplying the filtered GERB measurements  $L_{\text{GERB}}^f$  by the corresponding SEVIRI unfilter factor  $L_{\text{SEVIRI}}^{\text{uf}}/L_{\text{SEVIRI}}^f$  as

$$\begin{aligned} L_{\text{GERB}}^{\text{uf}} &= \left( \frac{L_{\text{SEVIRI}}^{\text{uf}}}{L_{\text{SEVIRI}}^f} \right) \cdot L_{\text{GERB}}^f \\ &= L_{\text{SEVIRI}}^{\text{uf}} \cdot \left( \frac{L_{\text{GERB}}^f}{L_{\text{SEVIRI}}^f} \right) = L_{\text{SEVIRI}}^{\text{uf}} \cdot C_L \end{aligned} \quad (3)$$

where  $L_{\text{GERB}}^f$  is the basic filtered BB GERB SW radiance measurement.  $L_{\text{SEVIRI}}^f$  is the estimate of the filtered BB

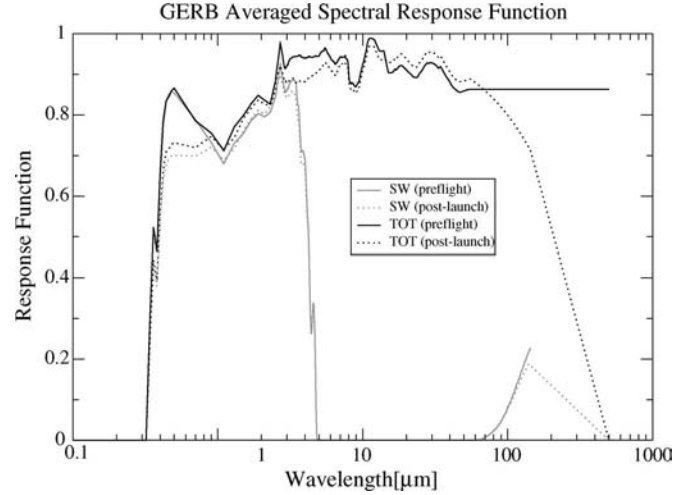


Fig. 1. Averaged spectral response functions of the GERB instrument. The prelaunch or laboratory measured values are given in black, while the gray lines indicate a postlaunch refined version.

GERB SW radiance measurement, which is estimated from the SEVIRI spectral radiances only.  $L_{\text{SEVIRI}}^{\text{uf}}$  is the corresponding estimate of the unfiltered BB radiance, which is estimated from the SEVIRI spectral radiances only.  $C_L$  is the pixel-dependent correction factor (CF) (i.e.,  $L_{\text{GERB}}^f/L_{\text{SEVIRI}}^f$ ) at the nominal GERB spatial resolution.

The BB SEVIRI filtered radiance  $L_{\text{SEVIRI}}^f$  and the SEVIRI unfilter factor  $L_{\text{SEVIRI}}^{\text{uf}}/L_{\text{SEVIRI}}^f$  are estimated from the SEVIRI imager through NB-to-BB conversion and convolution with the GERB point spread function (PSF). The spectral conversion (NB-to-BB) is performed by way of polynomial regressions on the NB radiances, i.e.,

$$\begin{aligned} L_{\text{SEVIRI}}^f &= a + b_1 L_{0.6 \mu\text{m}} + b_2 L_{0.8 \mu\text{m}} + b_3 L_{1.6 \mu\text{m}} \\ &\quad + c_{11} L_{0.6 \mu\text{m}}^2 + c_{21} L_{0.8 \mu\text{m}} L_{0.6 \mu\text{m}} \\ &\quad + c_{22} L_{0.8 \mu\text{m}}^2 + c_{31} L_{1.6 \mu\text{m}} L_{0.6 \mu\text{m}} \\ &\quad + c_{32} L_{1.6 \mu\text{m}} L_{0.8 \mu\text{m}} + c_{33} L_{1.6 \mu\text{m}}^2 \end{aligned} \quad (4)$$

$$\begin{aligned} L_{\text{SEVIRI}}^{\text{uf}} &= a' + b'_1 L_{0.6 \mu\text{m}} + b'_2 L_{0.8 \mu\text{m}} \\ &\quad + b'_3 L_{1.6 \mu\text{m}} + c'_{11} L_{0.6 \mu\text{m}}^2 + c'_{21} L_{0.8 \mu\text{m}} L_{0.6 \mu\text{m}} \\ &\quad + c'_{22} L_{0.8 \mu\text{m}}^2 + c'_{31} L_{1.6 \mu\text{m}} L_{0.6 \mu\text{m}} \\ &\quad + c'_{32} L_{1.6 \mu\text{m}} L_{0.8 \mu\text{m}} + c'_{33} L_{1.6 \mu\text{m}}^2 \end{aligned} \quad (5)$$

The regression coefficients in (4) and (5) are obtained from a regression analysis of theoretically derived filtered and unfiltered radiances. The simulated radiances are inferred from a spectral radiance database of Earth scenes generated by running the SBDART [16] radiative transfer model (RTM) for a large set of Earth-atmosphere conditions [6]. The radiative transfer computation was performed at 279 wavelengths that cover the solar spectrum and for 2310 conditions of the Earth-atmosphere system. For each element in the database, the main inputs for the radiative transfer computation were: 1) the Earth surface type characterized by its spectral albedo (four types of Earth's surfaces were considered: snow, ocean, sand, and vegetated surfaces; 2) the atmospheric profiles of temperature, pressure,

TABLE I  
REGRESSION COEFFICIENTS  $a$ ,  $b_i$ , AND  $c_{ij}$  (WHERE  $i, j = 1, 3$ ) USED IN (4) TO ESTIMATE THE SEVIRI BB  
FILTERED RADIANCE  $L_{\text{SEVIRI}}^f$  FROM THE SEVIRI SPECTRAL RADIANCE MEASUREMENTS.  
THE COEFFICIENTS ARE GIVEN AS A FUNCTION OF SZA  $\theta_s$

| $\theta_s$ | $a$   | $b_1$ | $b_2$ | $b_3$  | $c_{11}$ | $c_{21}$ | $c_{22}$ | $c_{31}$ | $c_{32}$ | $c_{33}$ |
|------------|-------|-------|-------|--------|----------|----------|----------|----------|----------|----------|
| 00         | 8.067 | 2.639 | 5.404 | -0.859 | -0.023   | 0.062    | 0.005    | 0.121    | -0.363   | 1.001    |
| 10         | 8.017 | 2.640 | 5.398 | -0.850 | -0.024   | 0.064    | 0.005    | 0.122    | -0.368   | 1.017    |
| 20         | 7.866 | 2.644 | 5.379 | -0.819 | -0.027   | 0.072    | 0.003    | 0.122    | -0.385   | 1.066    |
| 30         | 7.607 | 2.652 | 5.335 | -0.742 | -0.033   | 0.088    | 0.001    | 0.122    | -0.415   | 1.151    |
| 40         | 7.231 | 2.670 | 5.243 | -0.564 | -0.043   | 0.117    | -0.002   | 0.119    | -0.463   | 1.280    |
| 50         | 6.723 | 2.705 | 5.049 | -0.177 | -0.062   | 0.173    | -0.009   | 0.103    | -0.527   | 1.446    |
| 60         | 6.066 | 2.766 | 4.642 | 0.620  | -0.102   | 0.289    | -0.025   | 0.053    | -0.586   | 1.604    |
| 70         | 5.214 | 2.861 | 3.816 | 2.118  | -0.194   | 0.572    | -0.069   | -0.107   | -0.539   | 1.546    |
| 80         | 3.840 | 2.960 | 2.183 | 4.637  | -0.513   | 1.583    | -0.221   | -0.738   | 0.062    | 0.412    |
| 90         | 0.000 | 2.960 | 2.183 | 4.637  | -0.513   | 1.583    | -0.221   | -0.738   | 0.062    | 0.412    |

TABLE II  
REGRESSION COEFFICIENTS  $a'$ ,  $b'_i$ , AND  $c'_{ij}$  (WHERE  $i, j = 1, 3$ ) USED IN (5) TO ESTIMATE THE SEVIRI BB  
UNFILTERED SW RADIANCE  $L_{\text{SEVIRI}}^{\text{uf}}$  FROM THE SEVIRI SPECTRAL RADIANCE MEASUREMENTS.  
THE COEFFICIENTS ARE GIVEN AS A FUNCTION OF SZA  $\theta_s$

| $\theta_s$ | $a'$   | $b'_1$ | $b'_2$ | $b'_3$ | $c'_{11}$ | $c'_{21}$ | $c'_{22}$ | $c'_{31}$ | $c'_{32}$ | $c'_{33}$ |
|------------|--------|--------|--------|--------|-----------|-----------|-----------|-----------|-----------|-----------|
| 0          | 15.324 | 3.941  | 7.591  | -2.004 | -0.026    | 0.076     | 0.011     | 0.191     | -0.504    | 1.347     |
| 10         | 15.237 | 3.941  | 7.581  | -1.985 | -0.027    | 0.080     | 0.011     | 0.191     | -0.510    | 1.367     |
| 20         | 14.972 | 3.942  | 7.547  | -1.921 | -0.031    | 0.090     | 0.009     | 0.192     | -0.531    | 1.430     |
| 30         | 14.519 | 3.946  | 7.474  | -1.778 | -0.038    | 0.112     | 0.006     | 0.192     | -0.569    | 1.540     |
| 40         | 13.853 | 3.958  | 7.330  | -1.487 | -0.051    | 0.152     | 0.0002    | 0.186     | -0.625    | 1.702     |
| 50         | 12.937 | 3.984  | 7.043  | -0.908 | -0.077    | 0.229     | -0.010    | 0.163     | -0.698    | 1.909     |
| 60         | 11.706 | 4.030  | 6.470  | 0.207  | -0.128    | 0.388     | -0.033    | 0.092     | -0.755    | 2.098     |
| 70         | 9.986  | 4.093  | 5.346  | 2.210  | -0.245    | 0.766     | -0.092    | -0.122    | -0.658    | 2.001     |
| 80         | 7.081  | 4.124  | 3.160  | 5.455  | -0.641    | 2.085     | -0.258    | -0.922    | 0.143     | 0.570     |
| 90         | 0.000  | 4.125  | 3.160  | 5.455  | -0.641    | 2.085     | -0.258    | -0.922    | 0.143     | 0.570     |

water vapor, and ozone concentrations (they were extracted from the TIGR-3 database [5]); and 3) the cloud cover (which was generated randomly and may contain up to three overlapping layers, each characterized by a random height, optical thickness, phase, and drop size distribution). It is important to note that Clerbaux's database assumes Lambertian surfaces and does not represent the anisotropy due to broken cloud fields. Unfiltered radiances were determined by integrating spectral radiances over the appropriate wavenumber interval. In a similar way, filtered radiances are computed by integrating over the product of spectral radiance and spectral response function.

Because Lambertian surface reflectances were assumed when running the RTM to generate the spectral radiance database, the regression coefficients in (4) and (5) are neither dependent on the viewing zenith angle (VZA) nor on the relative azimuth angle (RAA) and vary only with the solar zenith angle (SZA). They were evaluated for ten SZAs independently of surface type and cloud conditions (Tables I and II). The error at  $1 - \sigma$  (RMSE) of the NB-to-BB fit (e.g.,  $L_{\text{SEVIRI}}^{\text{uf}}/L_{\text{SEVIRI}}^f$ ) to the theoretical calculations is of the order of 0.3% [10]. This value must be treated with caution, as it does not take into account the difference between the model and the data. The real error in unfiltering may therefore be significantly underestimated. The failure to include the full range of potential viewing conditions in the database used to derive the NB-to-BB fit through the use of Lambertian surface reflectance could therefore have the effect of producing an artificially low estimate of the RMSE error.

Note that the SEVIRI HRV channel is not used in the RMIB GERB SEVIRI processing (hereinafter, "RGSP") even though it covers a greater part of the SW spectrum than the three

separate spectral visible bands used to calculate the SEVIRI BB (un)filtered SW radiance. This is primarily to ensure spatial homogeneity in the flux computation within our processing, as the HRV channel covers only half of the full MS-8 disk in the EW direction. In addition, the geocoding accuracy for the HRV was found to be in the order of several pixels. Moreover, the HRV image is slightly warped, and the error, therefore, does not take the form of a simple translation.

### C. Radiance-to-Flux Conversion

Because spaceborne radiometers do not measure the Earth's outgoing fluxes directly, ADMs are required to relate the SW radiance actually measured to flux at a given solar angle, satellite-viewing geometry, and surface and atmospheric conditions, such that

$$F_{\text{SW}}(\theta_s) = \pi \cdot \frac{L_{\text{SW}}^{\text{uf}}(\theta_s, \theta_v, \phi)}{R_{\text{SW}}(\theta_s, \theta_v, \phi)} \quad (6)$$

where  $\theta_s$  and  $\theta_v$  are the SZA and VZA, respectively,  $\phi$  is the RAA, and finally,  $R_{\text{SW}}(\theta_s, \theta_v, \phi)$  is the BB SW ADM anisotropic CF.

The CERES-TRMM BB SW ADMs [13] are used to perform the SW radiance-to-flux conversion. The anisotropy of the Earth's scenes generally varies with the viewing geometry and the cloud/clear-sky properties in a continuous manner. However, CERES-TRMM ADMs are defined for discrete angular bins and scene types. Therefore, the CERES-TRMM anisotropic CFs (hereinafter, "ACFs") are adjusted to avoid introducing large instantaneous flux errors or sharp flux discontinuities between angular bins or scene types. Assuming

that the ADM ACF for a given scene type in a given angular bin corresponds to the midpoint of the discrete angular bin, we estimate ACFs by linearly interpolating the bin-averaged ACFs to each observation angle  $(\theta_s, \theta_v, \phi)$ .

The conversion of a footprint's BB radiance into the corresponding flux therefore requires that each footprint is characterized in terms of surface type and cloud cover properties (i.e., cloud fraction, cloud phase, and cloud optical depth) to properly select the adequate ADM. This information is retrieved from the spectral SEVIRI measurements (see [3] for further information). The Global Land Cover Map (version v1.2) produced by the International Geosphere Biosphere Program (IGBP, [2]) is used to select one of the six CERES classes (e.g., ocean, moderate-to-high vegetation, low-to-moderate vegetation, dark desert, bright desert, or ice/snow) for each SEVIRI pixel. This is done by merging the IGBP surface types into the CERES surface types.

Because the CERES BB radiometer footprint size on TRMM is about  $10 \text{ km} \times 10 \text{ km}$  at the subsatellite point,  $F_{\text{SEVIRI}}$  fluxes are not retrieved at the native SEVIRI resolution ( $3 \text{ km}$  at the subsatellite point). Instead, the GERB-like SEVIRI flux  $F_{3*SEVIRI}$  is estimated from the mean of  $3 \times 3$  SEVIRI pixel SW radiances using the appropriate CERES-TRMM ADMs based on the average scene identification (i.e., surface type and cloud properties) from the  $3 \times 3$  SEVIRI pixel box.

1) *Resolution Enhancement*: The resolution enhancement involves the enhancement of the GERB flux resolution to the high  $3 \times 3$  SEVIRI pixel resolution using the SEVIRI  $F_{3*SEVIRI}$  flux estimation. Basically, it relies on an upsampling<sup>1</sup> of the filtered GERB radiances from the nominal GERB footprint resolution ( $50 \text{ km}$  at nadir) to the  $3 \times 3$  SEVIRI pixel box resolution ( $9 \text{ km}$  at nadir). However, rather than directly interpolating the filtered GERB radiances, we use the CF  $C_L = L_{\text{GERB}}^f / L_{\text{SEVIRI}}^f$ , as introduced in (3). The CFs computed at the GERB nominal spatial resolution are spatially interpolated to derive CFs at the  $3 \times 3$  SEVIRI pixel resolution  $c_H$ .

In the first step, the fluxes at the GERB footprint resolution are derived from the  $3 \times 3$  SEVIRI-pixel-based flux estimates as

$$F_{\text{GERB}}(i, j) = \left( \sum_x \sum_y \text{PSF}(i, j, x, y) \cdot F_{3*SEVIRI}(x, y) \right) \cdot C_L(i, j) \quad (7)$$

where  $F_{\text{GERB}}(i, j)$  is the flux at the GERB footprint resolution  $(i, j = 1, \dots, m)$  and  $F_{3*SEVIRI}(x, y)$  is the flux at the  $3 \times 3$  SEVIRI pixel resolution  $(x, y = 1, \dots, n, \text{ with } n > m)$ .  $\text{PSF}(i, j, x, y)$  is the PSF of the GERB pixel  $(i, j)$ .

In the second step, the spatial resolution of the GERB fluxes is improved by the use of SEVIRI high-resolution information. Basically, this requires one to find CF  $c_H(x, y)$ , which, when applied to the high-resolution flux estimates, allows one to reproduce the low-resolution GERB fluxes after integration, i.e.,

$$F_{\text{GERB}}(i, j) = \sum_x \sum_y \text{PSF}(i, j, x, y) \cdot c_H(x, y) \cdot F_{3*SEVIRI}(x, y) \quad (8)$$

where  $c_H(x, y)$  is the CF at the high-resolution ( $3 \times 3$  SEVIRI pixel) or resolution-enhancement factor. Finally, the GERB flux at the  $3 \times 3$  SEVIRI pixel resolution is given by

$$F_{\text{GERB}/3*SEVIRI}(x, y) = c_H(x, y) \cdot F_{3*SEVIRI}(x, y). \quad (9)$$

2) *Temporal Averaging*: Because SEVIRI and GERB images are recorded at different times, a temporal matching between SEVIRI and GERB images is required prior to any comparison or combination of the two data types. First, SEVIRI data are interpolated (simple linear interpolation) to the GERB acquisition time, and the CFs are estimated at the GERB nominal spatial resolution  $C_L(i, j)$ . Then, in order to produce flux estimates at the SEVIRI acquisition time, a time-weighted average of the CF images over a 15-min time interval that is centered on the SEVIRI acquisition time is performed (e.g., time weighted of the 5.38-min GERB images of CF). Further information regarding the RMIB GERB-SEVIRI processing can be found in [3].

### III. DIURNAL ASYMMETRY

Fig. 2 presents the monthly mean (for April 2004) clear-sky SW flux difference at the high  $3 \times 3$  SEVIRI pixel resolution between the flux value at local noon and that at local noon  $\pm 2 \text{ h}$  for each footprint within the MS-8 FOV (color figure available at [ftp://gerb.oma.be/cedric/GERB\\_ASYM\\_Fig2\\_color.pdf](ftp://gerb.oma.be/cedric/GERB_ASYM_Fig2_color.pdf)). Morning differences and afternoon differences are displayed on the left-hand side and right-hand side of Fig. 2, respectively. The results are given for GERB (e.g.,  $F_{\text{GERB}/3*SEVIRI}$  in panels A and B) and GERB-like SEVIRI (e.g.,  $F_{3*SEVIRI}$  in panels C and D) data and for the corresponding CERES-TRMM ADMs flux values (panels E and F), respectively. For each footprint, local noon is taken as the time of minimum SZA on a 15-min slot basis. This explains why vertical line patterns are found in some areas and why the ADM morning and afternoon plots (panels E and F) are not exactly symmetric. More attention should therefore be given to the sign than to the magnitude of the flux differences shown in these panels. In an ideal situation (e.g., diurnally symmetric flux), the morning and afternoon flux differences will be positive, as illustrated in the ADM plots (panels E and F, respectively).

The negative patterns in Fig. 2 tend to indicate possible deficiencies in the GERB and GERB-like SW flux computations at least over a clear ocean surface. The negative patterns found over Africa (e.g., at the junction between the savanna and the green forest and over the African green forest area) probably originate from an erroneous cloud-screening procedure (e.g., cloudy footprints retrieved as clear). Further information regarding the cloud-screening algorithm applied can be found in [12]. Over the ocean surface, the asymmetry problem is most clearly apparent in the GERB-like SEVIRI fluxes (panels C and D). As an example, to the west of the disk, the maximum TOA reflected SW flux (equivalent to a minimum TOA albedo value) occurs after local noon (determined as the time of minimum SZA), so a positive flux difference is found before local noon (see panel C) and a negative one is found afterward (see panel D). Inversely, the maximum TOA reflected SW flux occurs before local noon in the eastern part of the disk, leading to a negative flux difference before local

<sup>1</sup>Upsampling is a process of generating intermediate samples between discrete samples.

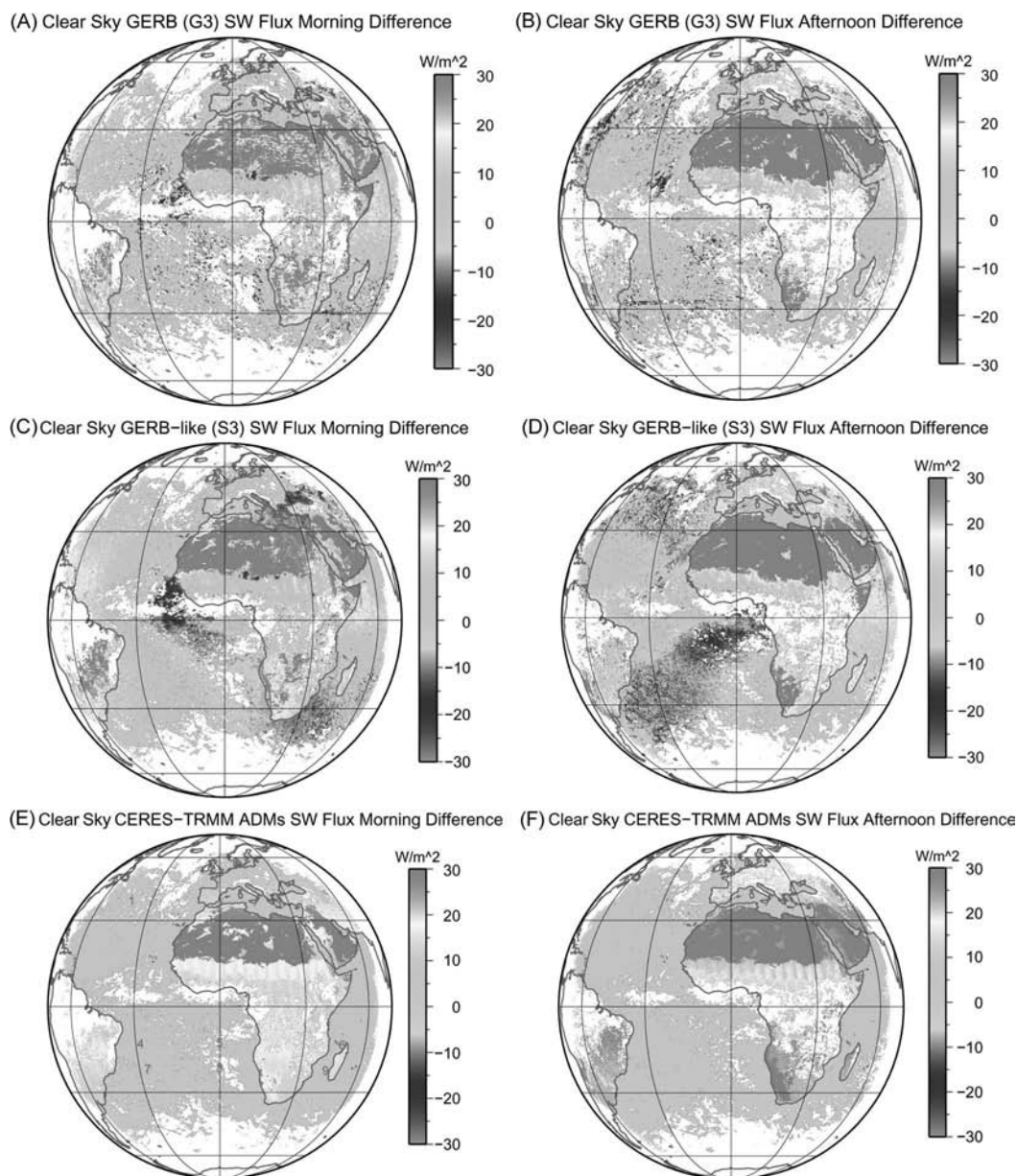


Fig. 2. Monthly mean (for April 2004) clear-sky SW flux differences between the  $3 \times 3$  SEVIRI pixel footprint SW flux values at local noon and at local noon  $\pm 2$  h. Panel A exhibits the difference between the GERB flux ( $F_{\text{GERB}/3 \times \text{SEVIRI}}$ ) values at local noon and at local noon minus 2 h, while panel B displays the flux difference between local noon and local noon plus 2 h. The same is shown in panels C and D but for the GERB-like SEVIRI fluxes ( $F_{3 \times \text{SEVIRI}}$ ). Similarly, panels E and F give the corresponding clear-sky CERES-TRMM ADMs SW flux differences at local noon  $\pm 2$  h. The flux difference is given in watts per square meter. In addition, the geographical locations of the nine selected ocean footprints in the SEVIRI FOV are indicated in panel E as follows: (1) [38.74N, 41.08W], (2) [37.00N, 0.00E], (3) [37.70N, 25.41E], (4) [11.97S, 28.09W], (5) [11.69S, 0.00E], (6) [12.43S, 46.78E], (7) [20.80S, 26.62W], (8) [20.36S, 0.00E], and (9) [21.37S, 41.29E]. (Color figure available at [ftp://gerb.oma.be/cedric/GERB\\_ASYM\\_Fig2\\_color.pdf](http://gerb.oma.be/cedric/GERB_ASYM_Fig2_color.pdf).)

noon (see panel C) and a positive one afterward (see panel D). While less marked than for the clear-ocean GERB-like SEVIRI fluxes, such trends can also be found in the GERB plots (panels A and B).

Fig. 3 displays the monthly mean diurnal evolution (from sunrise to sunset) of the GERB ( $F_{\text{GERB}/3 \times \text{SEVIRI}}$ ) and GERB-like SEVIRI ( $F_{3 \times \text{SEVIRI}}$ ) clear-sky SW fluxes (gray and black solid lines, respectively) for nine ocean footprints selected in the MS-8 FOV (see panel E in Fig. 2 for a spatial distribution of the footprints within the SEVIRI disk). The corresponding CERES-TRMM all-wind-speed clear-ocean ADM (ADM number 5) SW fluxes (dashed lines) are also shown for comparison. Because the asymmetry in the flux can

be masked by the large diurnal variation in the incoming solar flux, the monthly mean diurnal variation of the TOA albedo for the nine selected ocean footprints is provided in Fig. 4. As we can see, SW flux estimation from the SEVIRI NB radiance measurements over clear ocean footprints located in the western part of the SEVIRI FOV (solid black lines in panels 1, 4, and 7 in Fig. 3) exhibit an upward trend from sunrise to sunset. In contrast, GERB-like SEVIRI SW fluxes computed over eastern clear ocean footprints (solid black lines in the panels 3, 6, and 9 in Fig. 3) present a downward trend from sunrise to sunset. Such an upward/downward trend in the reflected SW flux at TOA is clearly not found in the ADM flux time series (dashed black lines in Fig. 3), which are instead quite symmetric around local

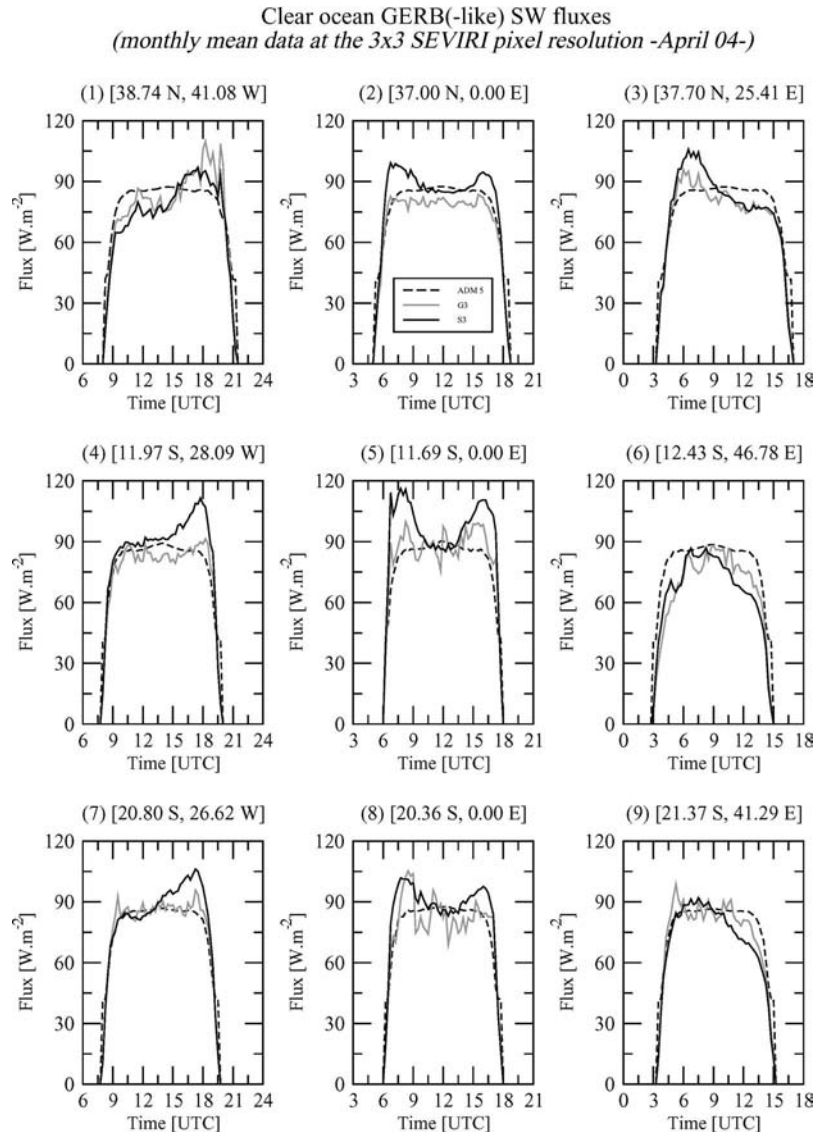


Fig. 3. Comparison between the diurnal evolutions (from sunrise to sunset) of the monthly mean clear-sky GERB (G3), GERB-like SEVIRI (S3), and corresponding CERES-TRMM ADM 5 (ADM) SW fluxes. The comparison is given for April 2004 and for the nine ocean footprints ( $3 \times 3$  SEVIRI pixel resolution) located within the SEVIRI FOV defined in Fig. 2 (panel E). The dashed lines are for the CERES-TRMM ADM 5 fluxes, while the solid gray and black lines are for the GERB and GERB-like SEVIRI fluxes, respectively.

noon whatever the footprint location within the MS-8 FOV may be. The magnitude of the GERB-like SEVIRI fluxes computed over clear footprints located in the middle part of the MS-8 FOV (solid black lines in panels 2, 5, and 8 in Fig. 3) appears to be overestimated during the morning and afternoon periods and somewhat underestimated at noon. In contrast, CERES-TRMM BB clear-ocean SW ADMs indicate an increased amount of reflected SW fluxes at local noon, as shown by the time evolution of the CERES-TRMM ADM 5 fluxes displayed in Fig. 3. Regarding the diurnal evolution of the estimated GERB SW fluxes, the gray lines in Fig. 3 indicate that the asymmetry problem is less systematic than that seen for the GERB-like SEVIRI fluxes. This is further apparent in Fig. 4, where the time evolution of the GERB TOA albedo appears to be more similar to the ADM time series than that found for GERB-like SEVIRI albedo. The high-frequency noise seen in the GERB and GERB-like data is due to cloud contamination, as discussed in Section III-B.

#### A. Normalization Factor and Aerosol Correction

It is worth pointing out that in addition to the adjustment of the ADM ACF applied prior to the performance of the radiance-to-flux conversion (6), the CERES algorithm accounts for an additional correction not originally implemented in the RGSP. This correction (the ADM normalization factor) allows the bias introduced in the mean flux when linear interpolation is used to adjust the ADM ACF (due to the fact that the actual ADM radiance varies nonlinearly within an angular bin) to be removed [13]. Moreover, because the anisotropy of clear ocean scenes depends on aerosol optical depth (AOD) (adding aerosols generally leads to a more isotropic ADM), the CERES algorithm also includes an aerosol correction when estimating the SW flux from the measured directional SW radiance over a clear ocean.

To assess the potential impact of these corrections on the GERB and GERB-like SEVIRI SW flux estimates (i.e., Are they able to solve the asymmetry found in the SW fluxes?), the reflected TOA SW flux over some selected clear ocean

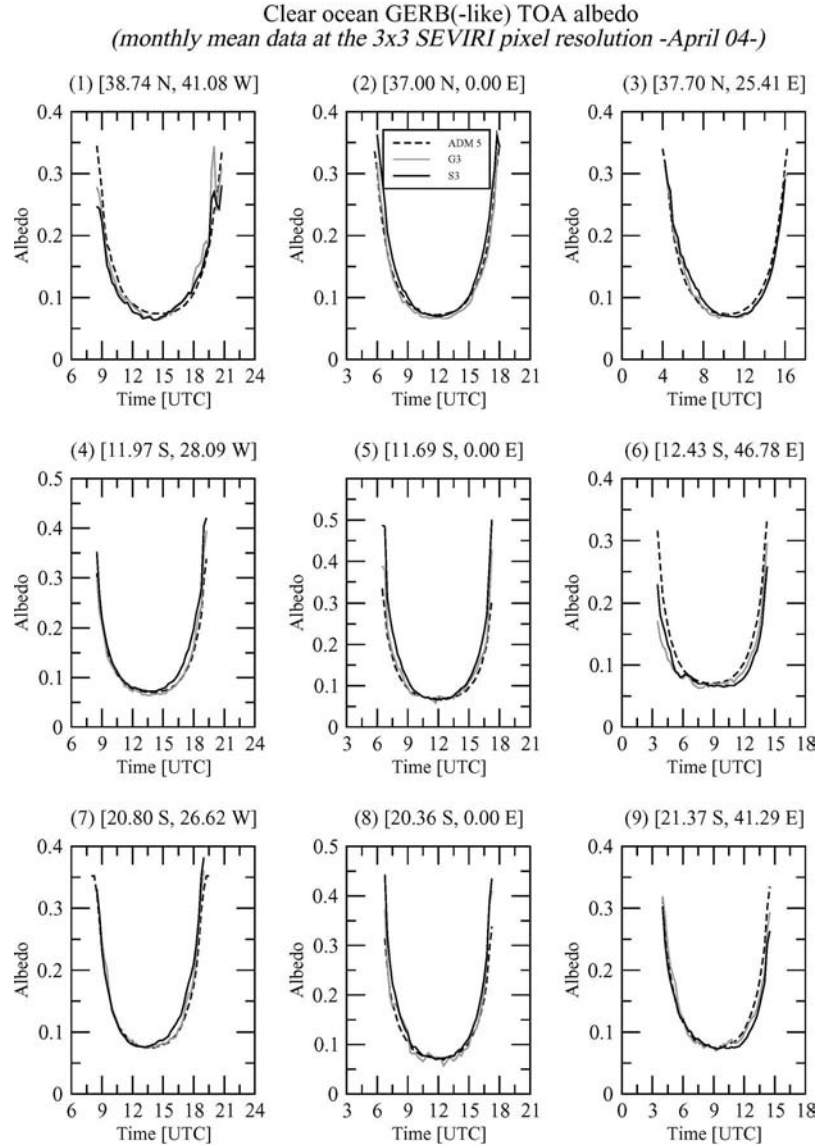


Fig. 4. Comparison between the diurnal evolutions (from sunrise to sunset) of the monthly mean clear-sky GERB (G3), GERB-like SEVIRI (S3), and corresponding CERES-TRMM ADM 5 (ADM) TOA albedo. The comparison is given for April 2004 and for the nine ocean footprints ( $3 \times 3$  SEVIRI pixel resolution) located within the SEVIRI FOV defined in Fig. 2 (panel E). The dashed lines are for the CERES-TRMM ADM 5 TOA albedo, while the solid gray and black lines are for the GERB and GERB-like SEVIRI TOA albedos, respectively.

footprints (at the  $3 \times 3$  SEVIRI pixel resolution) was recalculated according to the CERES formulation [13] as

$$F(\theta_s) = \frac{\pi L^*(\theta_s, \theta_v, \phi)}{\tilde{R}_j(w_j; \theta_s, \theta_v, \phi) \left[ \frac{R^{\text{th}}(w_j; L^*)}{R^{\text{th}}(w_j; \tilde{L})} \right]} + \delta F_j(w_j; \theta_s, \theta_v, \phi) \quad (10)$$

where the ADM-interpolated ACF  $\tilde{R}_j(w_j; \theta_s, \theta_v, \phi)$  is determined from the wind-speed-dependent ADM of scene type  $j$ .  $R^{\text{th}}(w_j; L^*)$  and  $R^{\text{th}}(w_j; \tilde{L})$  are the theoretical ACFs inferred from the measured radiance  $L^*(\theta_s, \theta_v, \phi)$  and the interpolated ADM radiance  $\tilde{L}(\theta_s, \theta_v, \phi)$ , respectively. Basically,  $R^{\text{th}}(w_j; L^*)$  and  $R^{\text{th}}(w_j; \tilde{L})$  are determined by comparing  $L^*(\theta_s, \theta_v, \phi)$  and  $\tilde{L}(\theta_s, \theta_v, \phi)$  with the lookup tables (LUTs) of theoretical SW radiances stratified by AOD in order to estimate the level of radiance contamination by aerosols. Hence,

$R^{\text{th}}(w_j; L^*)$  and  $R^{\text{th}}(w_j; \tilde{L})$  correspond to the AOD values for which the theoretical radiances match the measured and ADM radiances, respectively. Finally,  $\delta F_j(w_j; \theta_s, \theta_v, \phi)$  is the ADM normalization factor.

For the ADM aerosol correction to be implemented, wind speed information above the ocean surface is required. Unfortunately, this cannot be retrieved from the MS-8 platform. To overcome this difficulty, an invariant wind speed value of  $7 \text{ m} \cdot \text{s}^{-1}$  was applied. Fig. 5 presents for three of the nine selected ocean footprints (a western, central, and eastern ocean footprint, respectively), and given clear-sky days, the impact of the ADM aerosol correction and normalization in the time evolution of the high-resolution GERB and GERB-like SEVIRI SW fluxes. The numbers in brackets above each top panel in this figure indicate the footprint location within the MS-8 FOV, as given in Fig. 2 (panel E), and the associated dates provide the selected day. For each of the three ocean footprints, panels



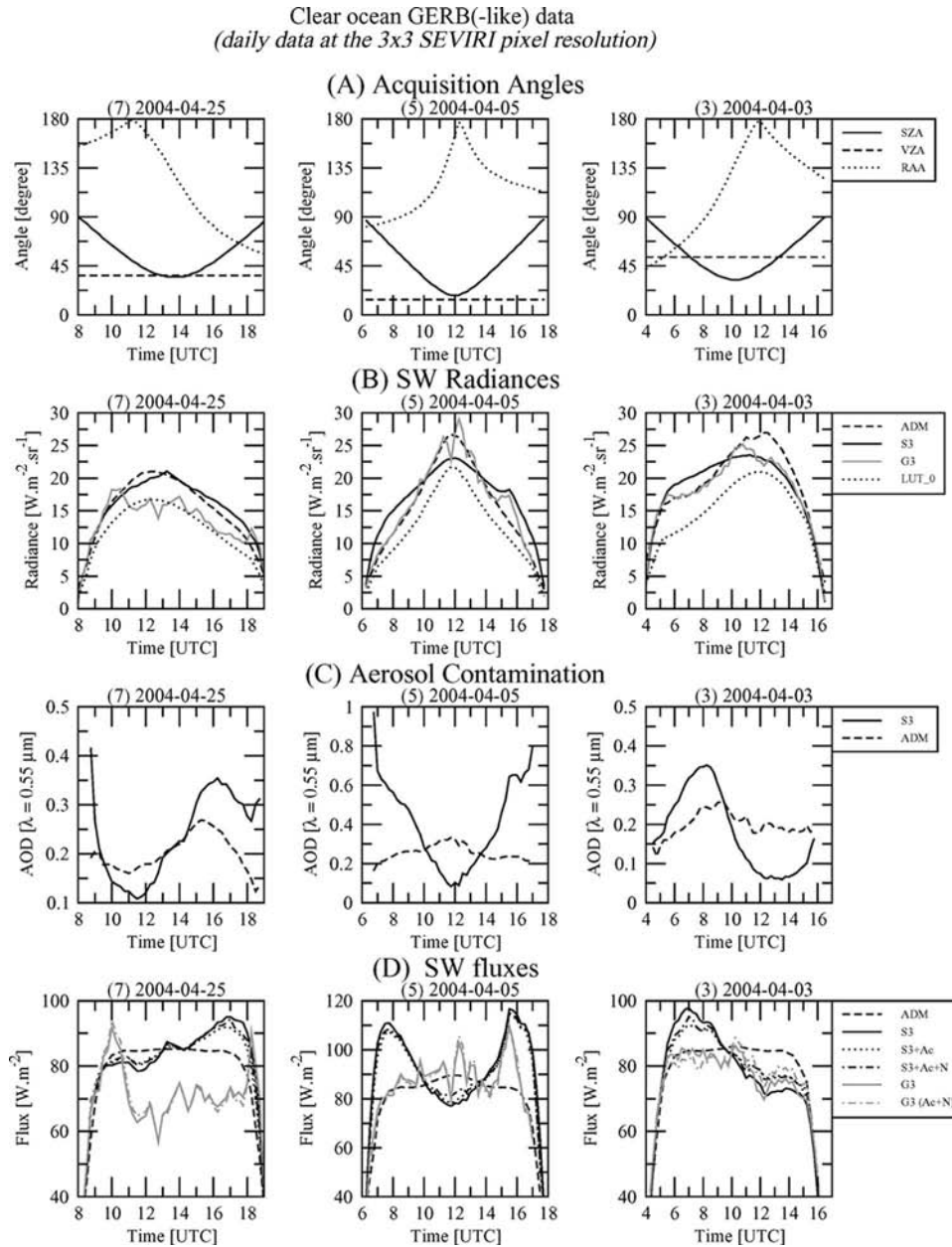


Fig. 5. Impact of the ADM aerosol correction and normalization on the estimated high-resolution GERB and GERB-like SEVIRI reflected clear-sky SW fluxes at TOA over the clear ocean surface. The numbers in brackets above each top panel indicate the footprint location within the SEVIRI FOV, as given in Fig. 2 (panel E), and the associated dates provide the selected day. Panels A display the time evolution of the footprint acquisition angles on the selected day (solar zenith angle, SZA; viewing zenith angle, VZA; relative azimuth angle, RAA). Panels B compare the diurnal evolutions of the GERB SW radiances (G3 in gray) and the estimated BB unfiltered SW SEVIRI radiances (S3 in black) for each of the three selected clear ocean footprints, together with the corresponding clear-ocean CERES-TRMM BB ADM 3 SW radiances (ADM dashed black lines) and the aerosol uncontaminated theoretical SW radiances (LUT\_0, dotted black lines). The retrieved levels of aerosol contamination in the estimated BB SEVIRI SW radiances and in the ADM radiances are provided in terms of AOD in panels C (the solid and dashed black lines, respectively). Finally, panels D compare the ADM flux (ADM dashed black line) time evolutions of the GERB (G3 in gray) and GERB-like SEVIRI (S3 in black) flux time series computed with and without accounting for the ADM aerosol correction and normalization. The solid lines are for fluxes computed without adding any corrections. The dotted line is for fluxes computed with the ADM aerosol corrections (Ac). The dotted-dashed lines are for fluxes computed with the ADM aerosol correction and normalization (Ac + N).

A display the time evolution of the footprint acquisition angles (e.g., SZA, VZA, and RAA) for the selected days, while the corresponding GERB and GERB-like SEVIRI SW radiances are given in panels B. The corresponding CERES-TRMM SW ADM 3 (clear-ocean ADM defined for a wind speed interval of approximately  $5.5\text{--}7.5\text{ m}\cdot\text{s}^{-1}$ ) radiances (dashed black lines) and the aerosols uncontaminated theoretical SW radiances (dotted black lines), as retrieved from the LUTs of theoretical

SW radiances used in the ADM aerosol correction process (10), (hereinafter, “reference LUT\_0 radiances”), are provided in panels B. Panels C give the level of the aerosol contamination (expressed in terms of AOD at  $\lambda = 0.55\text{ }\mu\text{m}$ ) inferred from the ADM radiances (dashed black lines) and the SEVIRI SW radiances (solid black lines), respectively.

The AOD values retrieved from the BB unfiltered SEVIRI SW radiances show a distinct diurnal cycle pattern with AOD



values of up to 0.8 (central panel C), which seems to be an artifact. In contrast, the ADM displays a reduced aerosol contamination in the SW radiances, which in addition does not vary much through the day for a given footprint (about  $\tau_{\text{aero}} \pm 0.05$ ). The fictitious sinusoidal shape of the AOD diurnal cycle found in the SEVIRI SW radiances appears to be a function of the sine of the RAA. Panels A in Fig. 5 indicate that the footprint acquisition geometry are mainly in the backward hemisphere, and panels C reveal that the aerosol contamination is minimum at  $\phi = 180^\circ$  when the SEVIRI SW radiances underestimate the ADM radiances and maximum at  $\phi = 90^\circ$  when the SEVIRI SW radiances overestimate the ADM radiances.

The comparison between the diurnal evolutions of the GERB and GERB-like SEVIRI SW fluxes in Fig. 5 (gray versus black lines in panels D) reveals that neither the aerosol correction (dotted line) nor the ADM normalization or their combination (dot-dashed line) is sufficient to solve the asymmetry problem found in our SW fluxes. Moreover, because the GERB flux is estimated in the RGSP by correcting the SEVIRI SW flux estimation with the SW CF (9) and not by directly converting the GERB SW radiance (i.e., the SEVIRI SW radiance corrected by the SW CF) into flux, the corrected GERB SW flux time series displayed in Fig. 5 (dotted-dashed gray lines in panels D) is not rigorously correct. Our use of (11) to estimate the high-resolution GERB SW flux implicitly leads to a modification in the ADM-dependent normalization factor  $\delta F_j$  value, which does not make sense physically. In addition, due to the ADM aerosol correction, estimation of the GERB SW flux using (11) or even its corrected form (12) will differ substantially from a radiance-to-flux conversion actually performed on the corrected SEVIRI BB SW radiances  $L_{3*SEVIRI} \cdot c_H$  (i.e., the GERB SW radiances), as in (13), because of the nonlinearity of the system, i.e.,  $F_{\text{calc}}(\theta_s) \neq F_{\text{cor}}(\theta_s) \neq F(\theta_s)$  or

$$F_{\text{calc}}(\theta_s) = \left( \frac{\pi L_{3*SEVIRI}(\theta_s, \theta_v, \phi)}{\tilde{R}_j(w_j; \theta_s, \theta_v, \phi) \left[ \frac{R^{\text{th}}(w_j; L_{3*SEVIRI})}{R^{\text{th}}(w_j; \tilde{L})} \right]} + \delta F_j(w_j; \theta_s, \theta_v, \phi) \right) \cdot c_H \quad (11)$$

$$F_{\text{cor}}(\theta_s) = \left( \frac{\pi L_{3*SEVIRI}(\theta_s, \theta_v, \phi)}{\tilde{R}_j(w_j; \theta_s, \theta_v, \phi) \left[ \frac{R^{\text{th}}(w_j; L_{3*SEVIRI})}{R^{\text{th}}(w_j; \tilde{L})} \right]} + \delta F_j(w_j; \theta_s, \theta_v, \phi) \right) \cdot c_H \quad (12)$$

$$F(\theta_s) = \frac{\pi (L_{3*SEVIRI}(\theta_s, \theta_v, \phi) \cdot c_H)}{\tilde{R}_j(w_j; \theta_s, \theta_v, \phi) \left[ \frac{R^{\text{th}}(w_j; L_{3*SEVIRI} \cdot c_H)}{R^{\text{th}}(w_j; \tilde{L})} \right]} + \delta F_j(w_j; \theta_s, \theta_v, \phi) \quad (13)$$

where  $\tilde{R}(w_j; \theta_s, \theta_v, \phi)$  is the ACF determined from the wind-speed-dependent clear-ocean CERES-TRMM ADMs.  $R^{\text{th}}(w_j; L_{3*SEVIRI})$ ,  $R^{\text{th}}(w_j; L_{3*SEVIRI} \cdot c_H)$ , and  $R^{\text{th}}(w_j; \tilde{L})$  are the theoretical ACFs inferred from the estimated SEVIRI BB SW radiance  $L_{3*SEVIRI}(\theta_s, \theta_v, \phi)$ , the corrected SEVIRI BB SW radiance estimation  $L_{3*SEVIRI}(\theta_s, \theta_v, \phi) \cdot c_H$ , and the interpolated ADM radiance

$\tilde{L}(\theta_s, \theta_v, \phi)$ .  $\delta F_j(w_j; \theta_s, \theta_v, \phi)$  is the ADM-dependent normalization factor.

The high AOD values and variabilities found in the estimated BB unfiltered SEVIRI SW radiances (solid lines panels C in Fig. 5) could indicate issues with our assumption of an invariant wind speed value of  $7 \text{ m} \cdot \text{s}^{-1}$  when retrieving the level of aerosol contamination as, this approach is not consistent with the scene identification technique used to derive the empirical CERES-TRMM ADMs. However, it is worth pointing out that the wind-speed dependence of the clear-ocean CERES-TRMM ADMs is essentially only an issue near sun glint (see, e.g., [4]). More probably, the AOD variability and magnitude are due to deficiencies in our NB-to-BB conversion. The use of Lambertian surface reflectance, which fails to include the full range of potential viewing conditions in the database of theoretical radiances, makes the ADM ACF adjustment sensitive to more than just the presence of aerosols.

### B. NB-to-BB Conversion and Unfiltering Weaknesses

The radiance plots in Fig. 6 show that the diurnal variation of the estimated SEVIRI BB SW radiances (solid black lines) does not look like that of the ADM radiances (dotted black lines), and the conversion to flux amplifies the difference, as highlighted in Fig. 3. Nevertheless, multiplying the unfiltered SEVIRI BB SW radiances by the SW CF  $c_H$  [namely, the resolution enhancement factor in (8) and (9)] allows part of the disagreement between the estimated and the ADM radiance time series to be removed (gray versus black solid lines in Fig. 6). The SW CFs  $c_H$  and  $C_L$  offer an efficient way to assess the effectiveness of our NB-to-BB process as a function of the acquisition angles and scene types. Fig. 7 presents for (1) all scene types and (2) the clear ocean surface found within the MS-8 FOV throughout a given day the bin-averaged CFs at the high and low resolutions as a function of (A) SZA, (B) VZA and, (C) RAA (the gray and black solid lines in Fig. 6, respectively). For each angle, the same discrete angular bins as those considered in the CERES-TRMM BB SW ADMs have been used. Note that while Fig. 7 presents results computed from all available GERB and SEVIRI slots from sunrise to sunset on April 25, 2004, essentially the same results are found for the other days of the month.

What is interesting and comforting to note in Fig. 7 is the very good agreement between  $c_H$  and  $C_L$  when averaged over all scene types (gray versus black solid lines in the left panels of Fig. 7). Clearly, this is no longer the case when focusing on the clear ocean surfaces (gray versus black solid lines in the right panels of Fig. 7). The slight difference between  $c_H$  and  $C_L$  reported in the left top panel A for the SZA discrete angular bin  $80^\circ$ – $90^\circ$  is an artifact as for computational handling,  $c_H$  has been set to 1 when undefined. In contrast, the differences between  $c_H$  and  $C_L$  over the clear ocean surface are due to the unavoidable cloud contamination of  $c_H$  over clear scenes. When determining  $C_L$  over clear ocean, only clear GERB SW radiances and thus (because of the larger GERB footprint size) clear SEVIRI SW radiances are involved in the computation. Unfortunately, this is not necessarily true when computing  $c_H$ , as a cloud-free zone at the  $3 \times 3$  SEVIRI pixel footprint does not automatically imply that it is still the case at the GERB nominal footprint resolution. Note that such a cloud

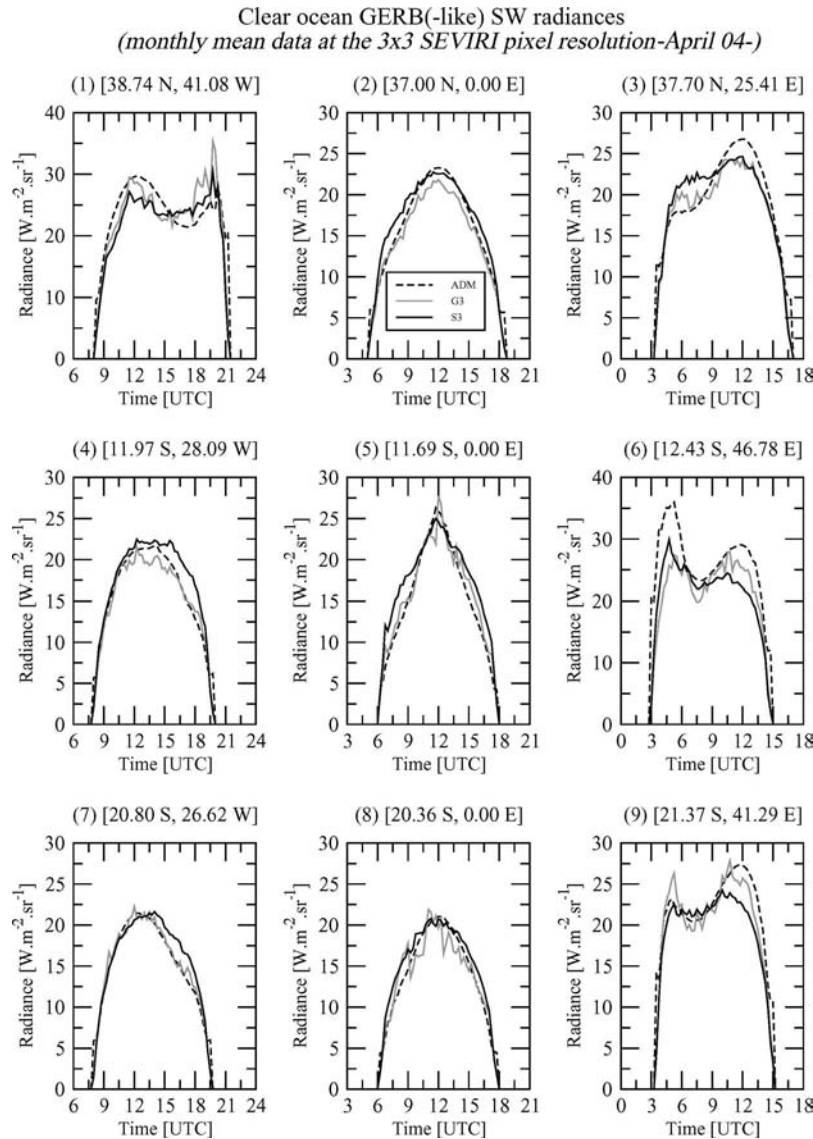


Fig. 6. Comparison between the diurnal evolutions (from sunrise to sunset) of the monthly mean clear-sky directional unfiltered GERB (G3), GERB-like SEVIRI (S3), and corresponding CERES-TRMM ADM 5 (ADM) SW radiances. The comparison is made for April 2004 and for nine ocean footprints ( $3 \times 3$  SEVIRI pixel resolution) located within the SEVIRI FOV, as defined in Fig. 2 (panel E). The dashed lines are for the CERES-TRMM ADM 5 radiances, while the solid gray and black lines are for the GERB and GERB-like SEVIRI radiances, respectively.

contamination in the clear-sky CF  $c_H$  occurs in all partly cloudy GERB footprints, regardless of surface type. Nevertheless, such contamination is likely to be more problematic above the clear ocean surface due to the enhanced albedo contrast between the cloud and the underlying dark surface. This cloud contamination of  $c_H$  over the clear ocean surface explains why the GERB SW radiance and flux time series displayed in Figs. 4 and 6 appear noisier than the corresponding SEVIRI SW radiances and fluxes (gray versus black solid lines in Figs. 4 and 6). Such contamination is also clearly apparent in the SW GERB radiance and flux time series displayed in Fig. 5 (gray lines in panels B and D, respectively).

Because the resolution enhancement is performed independently of the scene types and because the NB-to-BB equations have been derived independently of the cloud condition, the difference between  $c_H$  and  $C_L$  over clear scenes does not result from any systematic cloud retrieval errors (e.g., at low

zenith angles). The cloud contamination of  $c_H$  over clear scenes is thus a purely random process that is caused by the cloud contamination of the measured GERB radiance at the native GERB footprint resolution. In contrast, part of the noise in the monthly mean time series displayed in Figs. 3, 4, and 6 is due to some deficiencies in the cloud-screening procedure, as it can be detected in both the GERB and GERB-like SEVIRI time series. Finally, it is worth pointing out that the geolocation accuracy of the GERB SW filtered measurements may be reduced in the vicinity of sunrise and sunset as the amount of information available for geolocation computation dramatically decreases at those times.

The comparison between the left (all scenes) and right (clear ocean) panels in Fig. 7 reveals that the asymmetry problem we pointed out above the clear ocean surface may still be serious, although less obvious, in other scenes as a similar angular dependence is found in the bin-averaged CFs in the all-scene

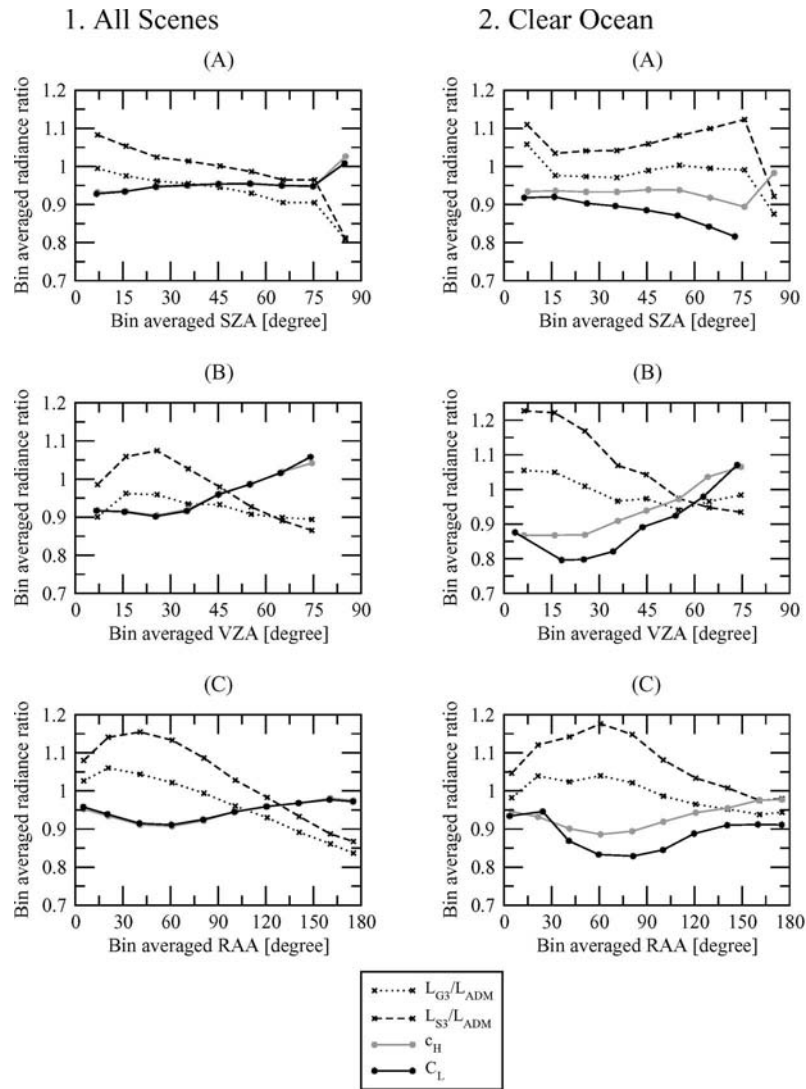


Fig. 7. Bin-averaged CF at high ( $C_H$ , solid gray lines) and low ( $C_L$ , solid black lines) resolutions as a function of (A) SZA, (B) VZA, and (C) RAA for (1) all scene types and (2) the clear ocean surface found within the MS-8 FOV for April 25, 2004. The bin-averaged ratios of the GERB and GERB-like SEVIRI high-resolution SW radiances to the corresponding CERES-TRMM ADM radiances ( $L_{G3}/L_{ADM}$  in dotted lines and  $L_{S3}/L_{ADM}$  in dashed black lines, respectively) are also plotted.

plots as in the clear-ocean plots (although the variation is a bit more pronounced in the latter case). This is not particularly surprising, as a single fit of coefficients is used for the NB-to-BB conversion (Tables I and II) for all scenes, regardless of surface type and cloud conditions. Panels B in Fig. 7 indicate that the CFs present a well-distinguishable angular dependence in VZA. Although of smaller magnitude, an angular dependence is also found in SZA (panels A) and RAA (panels C), where a concave and convex form, respectively, can be easily identified in the CFs time series.

The bin-averaged ratios of the GERB and SEVIRI SW radiances to the corresponding ADM radiance (e.g., the dotted and dashed black lines in Fig. 7, respectively) are also plotted in Fig. 7. Clearly, correcting the SEVIRI-based spectral modeling by the GERB SW measurement allows only part of the modeling errors and limitations (i.e., angular dependence) to be removed. In an ideal situation, the ratio of the GERB SW radiances to the corresponding radiance models derived from the CERES-TRMM data should be represented by a horizontal

line. Instead, a systematic angular dependence is found in all of the observation angles, although this is of reduced magnitude compared to what is observed for the uncorrected SEVIRI SW radiances (dotted versus dashed lines in Fig. 7) whatever the scene type may be.

#### IV. REFINED SPECTRAL MODELING APPROACH

To reduce the modeling errors and limitations inherent to the NB-to-BB conversion process, a new spectral modeling approach using empirical relations [8] was tested. These relations were derived from a database of coangular CERES BB SW radiances and spectral SEVIRI data. The CERES ERBE-like (ES8) Edition-2 data for the FM2 (on Terra) and FM3 (on Aqua) instruments for the months of March, April, and July 2004 were considered. The criteria used to select the data were based on: 1) the angle between the CERES and MS-8 direction of observations ( $\leq 3^\circ$ ); 2) the time difference between the SEVIRI and CERES observations ( $< 450$  s); 3) the spatial homogeneity

TABLE III  
REGRESSION COEFFICIENT  $c_i$  USED IN (14) TO PERFORM THE SURFACE-TYPE-DEPENDENT NB-TO-BB CONVERSION

| SURFACE       | $c_0$ | $c_1$ | $c_2$  | $c_3$ | $c_4$  | $c_5$    | $c_6$    |
|---------------|-------|-------|--------|-------|--------|----------|----------|
| Ocean         | 0.016 | 0.247 | 0.005  | 0.519 | 0.015  | 1.29E-04 | 2.65E-04 |
| Dark Vege.    | 0.007 | 0.448 | -0.018 | 0.373 | -0.008 | 3.79E-04 | 0.99E-04 |
| Bright Vege.  | 0.006 | 0.466 | -0.036 | 0.360 | -0.011 | 3.57E-04 | 1.69E-04 |
| Dark Desert   | 0.012 | 0.403 | 0.010  | 0.398 | -0.028 | 2.07E-04 | 1.32E-04 |
| Bright Desert | 0.037 | 0.239 | 0.075  | 0.478 | -0.070 | 5.66E-04 | 0.97E-04 |

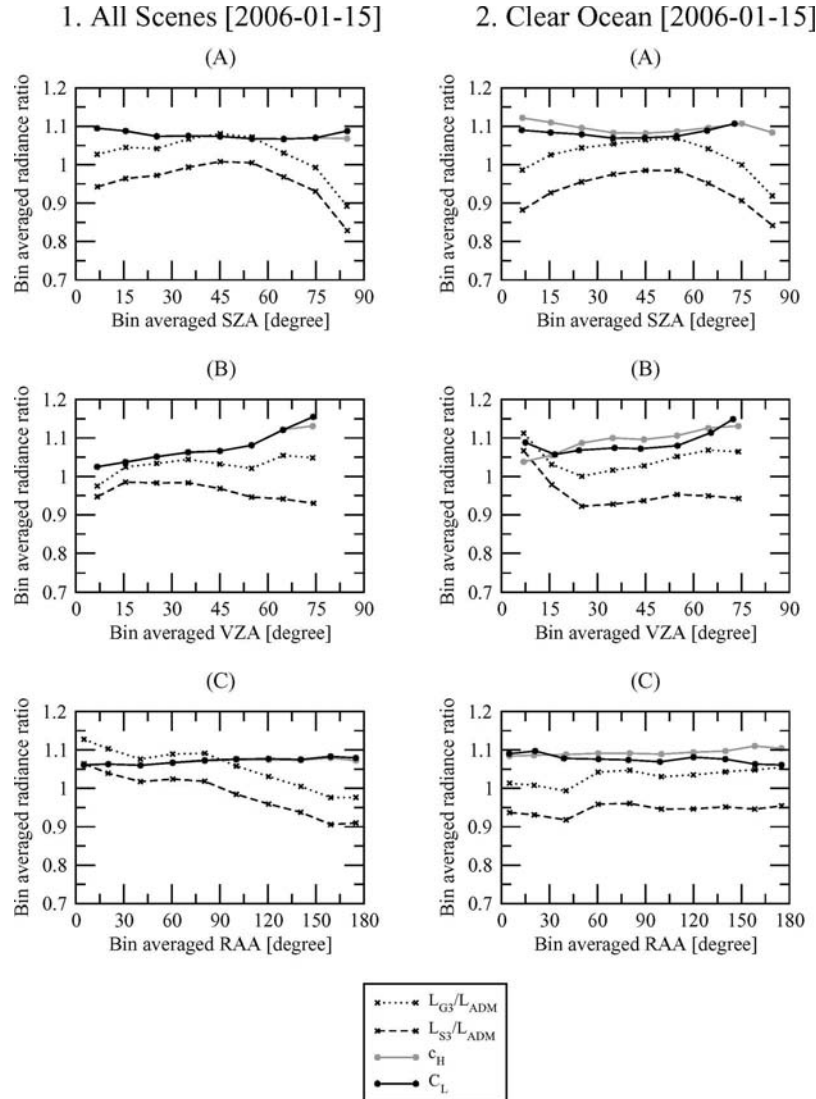


Fig. 8. Bin-averaged CF at high ( $C_H$ , solid gray lines) and low ( $C_L$ , solid black lines) resolutions as a function of (A) SZA, (B) VZA, and (C) RAA for (left) all scene types and (right) the clear ocean surface found within the MS-8 FOV for January 15, 2006. The bin-averaged ratios of the GERB and GERB-like SEVIRI high-resolution SW radiances to the corresponding CERES-TRMM ADM radiances ( $L_{G3}/L_{ADM}$  in dotted lines and  $L_{S3}/L_{ADM}$  in dashed black lines, respectively) are also plotted.

(the CERES PSF was modeled using a circular PSF with a radius of six SEVIRI pixels—about 18 km at the subsatellite point—and the spatial homogeneity in the neighborhood of the observations were estimated through the variation of the PSF averaged SEVIRI 0.6- $\mu\text{m}$  spectral values); and finally, 4) a glint angle (e.g., the angle between the reflected ray and the specular ray) that is larger than  $25^\circ$  in order to remove the risk of sun glint contamination. A NB-to-BB regression was derived independently of the cloud conditions for each of the following surface types: ocean, dark vegetation, bright vegetation, dark desert, and bright desert surfaces.

For each surface type, the regressions have the following form:

$$L_{\text{SEVIRI}}^{\text{uf}} = c_0 + c_1 L_{0.6\mu\text{m}} + c_2 L_{0.6\mu\text{m}}^2 + c_3 L_{0.8\mu\text{m}} + c_4 L_{1.6\mu\text{m}} + c_5 \theta_s + c_6 \gamma \quad (14)$$

where  $\theta_s$  is the SZA and  $\gamma$  is the sun glint angle [ $\cos \gamma = \mu_s \mu_v + \sqrt{(1 - \mu_s^2)(1 - \mu_v^2)} \cos(\phi)$ ], where  $\mu_s$  and  $\mu_v$  are the cosines of the SZA and VZA, respectively, and  $\phi$  is the RAA. Table III provides the regression coefficient  $c_i$  ( $i = 1, \dots, 6$ ) for each of the five NB-to-BB equations.

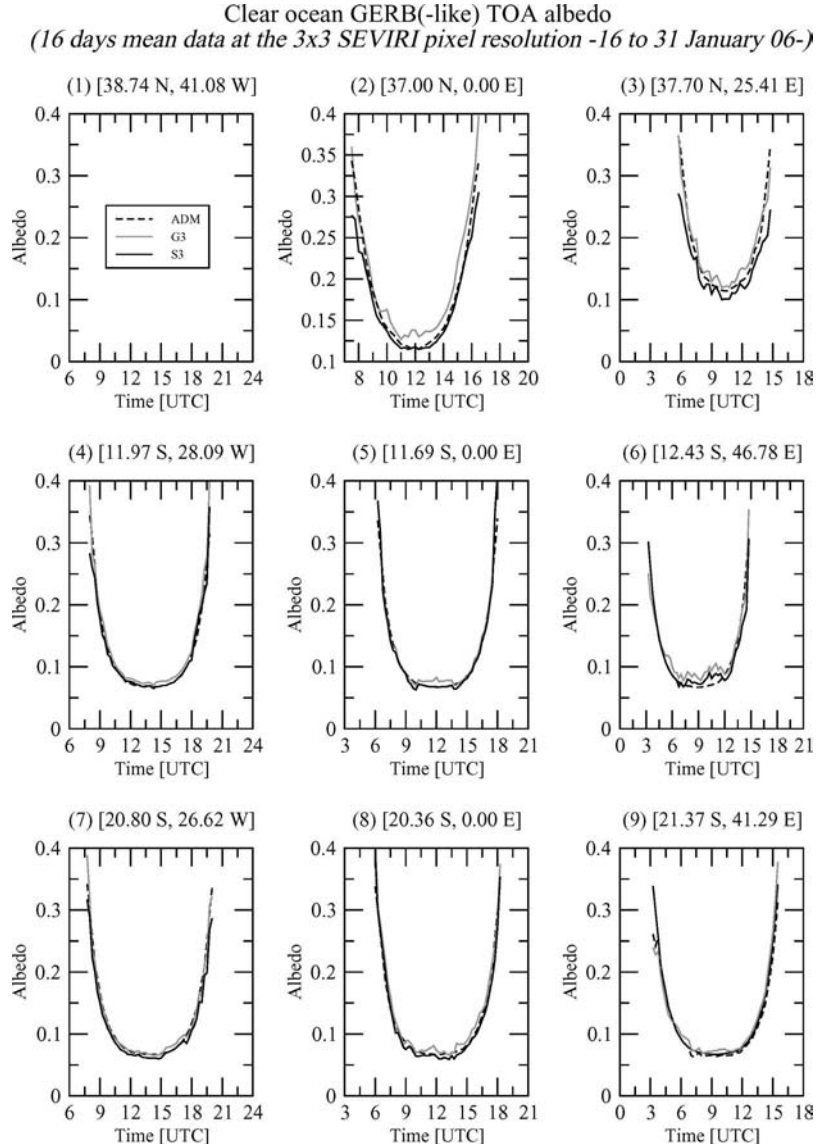


Fig. 9. Comparison between the diurnal evolutions (from sunrise to sunset) of the 16-day mean (January 15–31, 2006) clear-sky GERB (G3), GERB-like SEVIRI (S3), and corresponding CERES-TRMM ADM (ADM) TOA albedo. The comparison is given for eight of the nine ocean footprints ( $3 \times 3$  SEVIRI pixel resolution) located within the SEVIRI FOV defined in Fig. 2 (panel E). The dashed lines are for the CERES-TRMM ADM TOA albedo, while the solid gray and black lines are for the GERB and GERB-like SEVIRI TOA albedo, respectively.

Because Clerbaux *et al.* [8] reported a large NB-to-BB error of about 5% (up to 10% at grazing observation angles and at the subsatellite point) for the ocean surface, a CF [7] was applied to the NB-to-BB conversion over the clear ocean surface. It is defined as being the difference between the clear-ocean CERES-TRMM ADM 3 BB SW radiance  $L_{\text{ADM}}$  and the corresponding median value (the percentile at 50%) of the  $L_{\text{OCEAN}}^{\text{uf}}$  estimations from (14) using theoretical filtered SEVIRI spectral radiances at 0.6, 0.8, and  $1.6 \mu\text{m}$ , which were obtained from a total of 153 SBDART RTM simulations, i.e.,

$$C(\theta_s, \theta_v, \phi) = L_{\text{ADM}}(\theta_s, \theta_v, \phi) - L_{\text{OCEAN},50\%}^{\text{uf}}(\theta_s, \theta_v, \phi). \quad (15)$$

The correction is simply added to the estimated high-resolution SEVIRI BB unfiltered SW radiances over the clear ocean surface obtained from (14).

Because it is not possible to derive empirical relations to estimate the SEVIRI BB filtered SW radiances from a database of coangular CERES and SEVIRI data,  $L_{3*SEVIRI}^f$  was estimated as follows:

$$L_{3*SEVIRI,j}^f = L_{3*SEVIRI,j}^{\text{uf}} / \alpha_{\text{th},j} \quad (16)$$

where  $L_{3*SEVIRI,j}^{\text{uf}}$  is the estimate of the SEVIRI BB unfiltered SW radiance over the surface of type  $j$ , as given by (14) (with the addition of a correction term  $C(\theta_s, \theta_v, \phi)$  in case of the clear ocean surface), and  $\alpha_{\text{th},j}$  is a theoretical unfilter factor ( $L_{\text{th}_SEVIRI,j}^{\text{uf}} / L_{\text{th}_SEVIRI,j}^f$ ) calculated from a database of theoretical spectral radiances that are very similar to the one used to derive the regression coefficient in (4) and (5) (the major change rely on the inclusion of a [9] scheme for simulating ocean surface roughness).

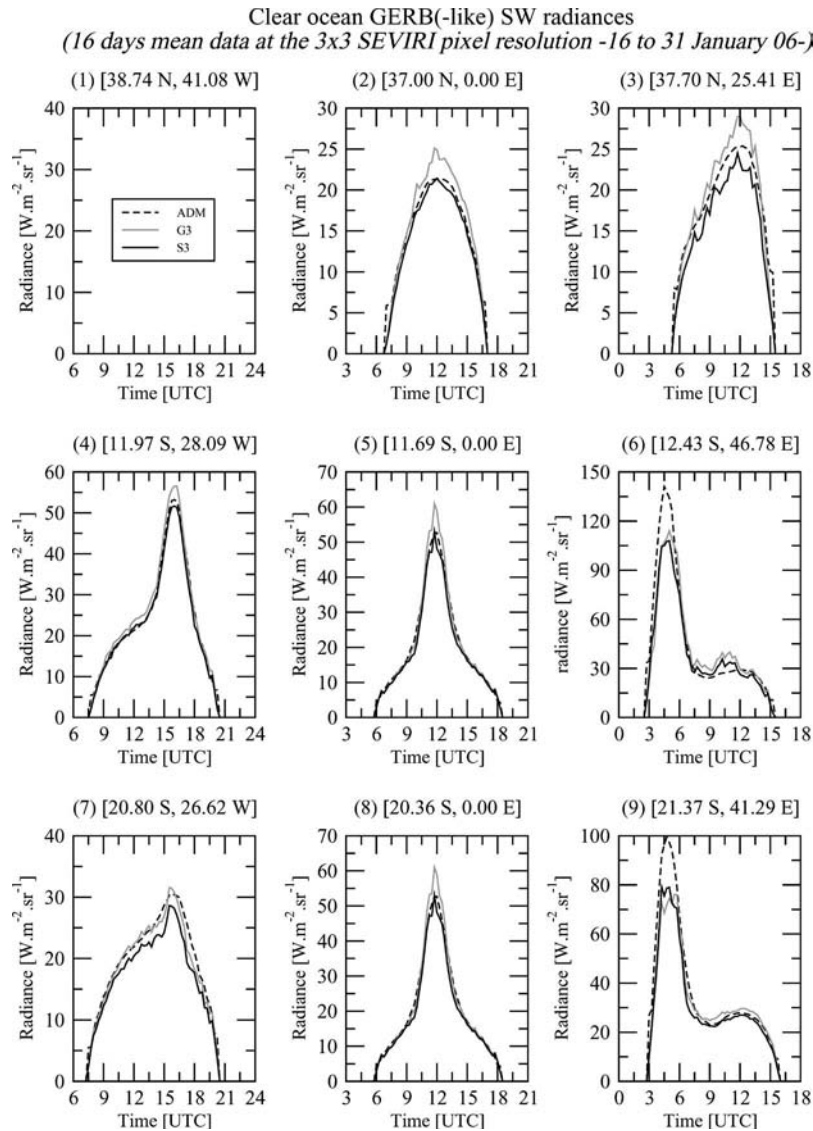


Fig. 10. Comparison between the diurnal evolutions (from sunrise to sunset) of the 16-day mean (January 15–31, 2006) clear-sky directional unfiltered GERB (G3), GERB-like SEVIRI (S3), and corresponding CERES-TRMM ADM (ADM) SW radiances. The comparison is made for eight of the nine ocean footprints ( $3 \times 3$  SEVIRI pixel resolution) located within the SEVIRI FOV, as defined in Fig. 2 (panel E). The dashed lines are for the CERES-TRMM ADM radiance, while the solid gray and black lines are for the GERB and GERB-like SEVIRI radiances, respectively.

### A. Results

The new SEVIRI spectral modeling was incorporated within the RGSP in mid-January 2006, together with the refined post-launch GERB spectral response functions provided by Imperial College, London, U.K. The comparison between the averaged preflight and refined postlaunch GERB spectral response functions in Fig. 1 (solid versus dotted lines, respectively) indicates that the magnitude of the GERB SW radiances could have been underestimated when using the uncorrected preflight calibration. Indeed, both the preflight and postlaunch spectral response functions are from the same preflight measurements; the difference is the measurements were corrected for artifacts in the original measurements that were only discovered postlaunch.

Similar to Fig. 7, Fig. 8 displays the bin-averaged CFs as a function of (A) SZA, (B) VZA, and (C) RAA for both (1) all scenes and (2) the clear ocean surface from all the available MS-8 slots on January 15, 2006. It appears from Fig. 8 that except in VZA (panels B), the angular dependence of  $c_H$  (solid

gray line) and  $C_L$  (solid black line) in SZA (panels A) and RAA (panels C) has been largely reduced in both the all-scene plots (left panels) and clear-ocean plots (right panels). While noticeably reduced over the clear ocean surface compared to that found with the previous spectral modeling scheme, an angular dependence in VZA of  $c_H$  and  $C_L$  is still apparent in Fig. 8 (gray and black solid lines in panels B).

Analysis of the bin-averaged ratio of the estimated SEVIRI BB unfiltered SW radiances with the corresponding ADM values for the clear-ocean case indicates that at least in SZA (dashed line in right panel A in Fig. 8) and in the first two discrete angular bins in VZA (dashed line in right panel B in Fig. 8), an angular dependence is still observed in spite of the angular-dependent correction applied to (14) for the clear ocean surface. Correcting the SEVIRI-based spectral modeling with the GERB SW measurement does not actually remove all the angular dependence, rather it tends to increase the SEVIRI BB SW radiances by 8%–10%. The situation does not differ

too much when focusing on the all-scene plots (dotted versus dashed lines in the left panels in Fig. 8). Presumably, the apparent poor correction by GERB originates from the lack of functionality of the theoretical unfilter factor  $\alpha_{th,j}$  [see (16)], with azimuth and VZA as well as with the cloud condition. Over the clear ocean surface, the problem could also be related to the cloud contamination of the clear-sky SW CF  $c_H$  and to the assumed SW spectral response of the GERB detectors [note the relatively large modification between the preflight and postlaunch averaged GERB SW spectral response functions displayed in Fig. 1 (solid versus dotted gray lines)] but is unlikely to result from limitations in the spectral modeling, as the new RTM simulations account the ocean surface roughness. The magnitude of the GERB SW radiances over the clear ocean surface could be overestimated when using the refined postlaunch SW spectral functions.

Nevertheless, because of the improved NB-to-BB conversion, the asymmetry problem in the SEVIRI BB unfiltered SW radiances is reduced, leading to an improvement in our estimated GERB SW flux values. This asymmetry reduction is clearly apparent in the 16-day mean (January 15–31) diurnal evolution of the clear-sky GERB and GERB-like SEVIRI TOA albedo displayed in Fig. 9 (gray and black lines, respectively) for eight of the nine ocean footprints previously selected (16 days being insufficient to retrieve clear-sky data on a 15-min slot basis for all the selected ocean footprints). The comparison with the corresponding CERES-TRMM ADM TOA albedo values reveals a quite good agreement in the time evolution of the GERB and the ADM (gray versus dashed black lines) data except in panel 2. Errors in the GERB geolocation could be an issue here as the SEVIRI estimates do not differ much from the ADM values (solid versus dashed black lines). Part of the noise in the GERB time series (e.g., panels 3 and 6) certainly originates from cloud contamination in the retrieved clear SW radiances (Fig. 10) due to erroneous cloud-screening detection, as similar fluctuations are found in the GERB-like SEVIRI data. Finally, the signature of a sun glint contamination in the SW radiances (Fig. 10) can also be identified in the GERB and GERB-like SEVIRI TOA albedo time series in Fig. 9 (e.g., panel 5).

## V. FINAL DISCUSSION AND CONCLUSION

Analysis of the diurnal variation of SW flux as observed from the GERB instrument has highlighted an unexpected asymmetry that is inconsistent with the flux models derived from the CERES data. While this is most apparent over clear oceanic regions, our analysis indicates that although the problem is less obvious in other scenes, it may still be serious. Scrutinizing the method implemented at RMIB to calculate the GERB SW fluxes from a combined use of SEVIRI and GERB data, we found that the primary cause of the problem is the SEVIRI spectral modeling. The use of Lambertian surface reflectance in the theoretical RTM simulations, from which the NB-to-BB conversion was derived, is a major issue as the NB-to-BB ratios can be dependent on viewing geometry. The lack of functionality with azimuth and VZA appears to be a major contributor to the large asymmetries found. The use of a single fit of coefficients for all scenes, independent of surface type and cloud conditions, in the NB-to-BB conversion of the SEVIRI radiances is also a major issue. Empirically derived surface-

type-dependent NB-to-BB equations have shown their usefulness in the reduction of the asymmetry problem. Separating clear from cloudy conditions in the surface-type-dependent NB-to-BB conversion will certainly improve the effectiveness of the SEVIRI spectral modeling and will presumably remove the need for a correction term over clear ocean surfaces. Uncertainty in the GERB detector spectral response functions could also be an issue. Work is ongoing within the GERB project team to address these remaining data quality issues.

Deficiencies in the cloud-screening algorithm (e.g., cloud-contaminated radiance retrieved as clear) and, hence, in the scene identification essentially lead to add a high-frequency variability (noise) in the GERB and GERB-like time series rather than contribute to the systematic asymmetry in the diurnal evolution of the SW fluxes. While being a random process, the unavoidable cloud contamination in the clear-sky SW CF at the high  $3 \times 3$  SEVIRI pixel resolution is more problematic as the efficiency of GERB in correcting the SEVIRI spectral modeling is reduced. This could be a nonnegligible issue, especially over dark scenes due to the enhanced albedo contrast between the cloud and the underlying surface. Accounting for a scene-type-dependent resolution enhancement process within the RGSP will allow to solve the cloud contamination in the clear-sky CF  $c_H$ . Additionally, due to GERB geolocation issues, the SW CF can be contaminated by numerical noise (e.g., in coastal zone, in the vicinity of sunrise and sunset, and at the cloud edges), which unfortunately impacts on the GERB SW flux estimation.

Because of the structure of the RGSP algorithm and the unavoidable lack of consistency with the CERES scene identification technique regarding wind-speed estimation, implementing the interpolation adjustment in the clear-ocean CERES-TRMM BB SW ADMs to account for the SW radiance aerosol contamination is not recommended. In contrast, the ADM normalization factor has been implemented in the RGSP. Finally, confirmation of the corrections applied to the GERB detectors spectral response functions will ensure that part of the remaining asymmetry is not due to the use of inappropriate spectral response functions within the RGSP.

## ACKNOWLEDGMENT

The authors would like to thank N. Loeb (Hampton University/NASA Langley Research Center, Hampton, VA) for providing them with the CERES-TRMM SW ADMs and for the very useful comments and remarks regarding the CERES-TRMM ADM corrections; and J. E. Russell and H. Brindley (Space and Atmospheric Blackett Laboratory, Imperial College, London, U.K.) for providing them with the GERB spectral response functions and for the constructive discussions. They would also like to thank the anonymous reviewers for their very constructive comments and suggestions.

## REFERENCES

- [1] B. R. Barkstrom, E. F. Harrison, G. L. Smith, R. Green, J. Kibler, and R. Cess, "Earth Radiation Budget Experiment (ERBE) archival and April 1985 results," *Bull. Amer. Meteorol. Soc.*, vol. 70, no. 10, pp. 12540–12620, Oct. 1989.
- [2] A. S. Belward, J. E. Estes, and K. D. Kline, "The IGBP-DIS 1-km land-cover data set DISCover: A project overview," *Photogramm. Eng. Remote Sens.*, vol. 65, no. 9, pp. 1013–1020, 1999.



- [3] C. Bertrand, D. Caprion, N. Clerbaux, S. Dewitte, L. Gonzalez, and A. Ipe, "First TOA fluxes from the Geostationary Earth Radiation Budget (GERB) instrument," in *Proc. SPIE Serie*, K. P. Schäfer, A. Comerón, M. R. Carleer, R. H. Picard, and N. I. Sifakis, Eds, 2004, vol. 5571, pp. 67–77.
- [4] C. Bertrand, N. Clerbaux, A. Ipe, S. Dewitte, and L. Gonzalez, "Angular distribution models anisotropic correction factors and sun glint: A sensitivity study," *Int. J. Remote Sens.*, vol. 27, no. 9, pp. 1741–1757, 2006.
- [5] F. Chevallier, A. Chédin, F. Chérut, and J. J. Morcrette, "TIGR-like atmospheric profile database for accurate radiative flux computation," *Q. J. R. Meteorol. Soc.*, vol. 126, no. 563, pp. 777–785, Jan. 2000.
- [6] N. Clerbaux, "Generation of a database of TOA spectral radiance fields," Roy. Meteorol. Inst. Belgium, Brussels, Belgium, Tech. Note MSG-RMIB-GE-TN-0030, 2004.
- [7] —, "Clear Ocean Correction for SEVIRI NB-to-BB Conversion," Roy. Meteorol. Inst. Belgium, Brussels, Belgium, Tech. Note MSG-RMIB-GE-TN-0037, 2006.
- [8] N. Clerbaux, C. Bertrand, D. Caprion, B. De Paepe, S. Dewitte, L. Gonzalez, and A. Ipe, "Narrowband-to-broadband conversions for SEVIRI," in *Proc. EUMETSAT Meteorological Satellite Conf.*, Dubrovnik, Croatia, Sep. 19–23, 2005, pp. 351–357.
- [9] C. Cox and W. Munk, "Measurements of the roughness of the sea surface from photographs of the Sun's glitter," *J. Opt. Soc. Amer.*, vol. 44, no. 11, pp. 838–850, 1954.
- [10] J. E. Harries, J. E. Russell, J. A. Hanafin, H. Brindley, J. Futyan, J. Rufus, S. Kellock, G. Matthews, R. Wrigley, A. Last, J. Mueller, R. Mossavati, J. Ashmall, E. Sawyer, D. Parker, M. Caldwell, P. M. Allan, A. Smith, M. J. Bates, B. Coan, B. C. Stewart, D. R. Lepine, L. A. Cornwall, D. R. Corney, M. J. Ricketts, D. Drummond, D. Smart, R. Cutler, S. Dewitte, N. Clerbaux, L. Gonzalez, A. Ipe, C. Bertrand, A. Joukoff, D. Crommelynck, N. Nelms, D. T. Llewellyn-Jones, G. Butcher, G. L. Smith, Z. P. Szewczyk, P. E. Mlynarczyk, A. Slingo, R. P. Allen, and M. Ringer, "The Geostationary Earth Radiation Budget Experiment (GERB)," *Bull. Amer. Meteorol. Soc.*, vol. 86, no. 7, pp. 945–960, 2005.
- [11] F. B. House, A. Gruber, G. E. Hunt, and A. T. Mecherikunnel, "History of satellite missions and measurements of the Earth radiation budget (1957–1984)," *Rev. Geophys.*, vol. 24, pp. 357–377, May 1986.
- [12] A. Ipe, C. Bertrand, N. Clerbaux, S. Dewitte, and L. Gonzalez, "Validation and homogenization of cloud optical depth and cloud fraction retrievals for GERB/SEVIRI scene identification using Meteosat-7 data," *Atmos. Res.*, vol. 72, no. 1–4, pp. 17–37, Nov. 2004.
- [13] N. G. Loeb, N. M. Smith, S. Kato, W. F. Miller, S. K. Gupta, P. Minnis, and B. A. Wielicki, "Angular distribution models for top-of-atmosphere radiative flux estimation from the clouds and the Earth's radiative flux estimation from the clouds and the Earth's radiant energy system instrument on the tropical rainfall measuring mission satellite—Part I: Methodology," *J. Appl. Meteorol.*, vol. 42, no. 2, pp. 240–265, 2003.
- [14] R. Mossavati, J. E. Harries, S. Kellock, R. T. Wrigley, J. Mueller, and N. P. Fox, "Radiometric calibration of the GERB instrument," *Meteorologica*, vol. 35, no. 4, pp. 603–607, Aug. 1998.
- [15] E. Raschke, T. H. Vonder Haar, W. R. Bandeen, and M. Pasternak, "The annual radiation balance of the Earth-atmosphere system during 1969–1970 from Nimbus-3 measurements," *J. Atmos. Sci.*, vol. 30, no. 3, pp. 341–364, 1973.
- [16] P. Ricchiazzi, S. Yang, C. Gautier, and D. Sowle, "SBDART: A research and teaching software tool for plane-parallel radiative transfer in the Earth's atmosphere," *Bull. Amer. Meteorol. Soc.*, vol. 79, no. 10, pp. 2101–2114, 1998.
- [17] J. Schmetz, P. Pili, S. Tjemkes, D. Just, J. Kerkmann, S. Rota, and A. Ratier, "An introduction to meteosat second generation (MSG)," *Bull. Amer. Meteorol. Soc.*, vol. 83, no. 7, pp. 977–992, 2002.
- [18] J. Schmetz, M. König, P. Pili, S. Rota, A. Ratier, and S. Tjemkes, "Meteosat Second Generation (MSG): Status after launch," presented at the 12th Conf. Satellite Meteorology and Oceanography, Long Beach, CA, Feb. 10–13, 2003.
- [19] B. A. Wielicki, B. R. Barkstrom, B. A. Baum, T. P. Charlock, R. N. Green, D. P. Kratz, R. B. Lee, P. Minnis, G. L. Smith, T. Wong, D. F. Young, R. D. Cess, J. A. Coakley, Jr., D. A. H. Crommelynck, L. Donner, R. Kandel, M. D. King, A. J. Miller, V. Ramanathan, D. A. Randall, L. L. Stowe, and R. M. Welch, "Clouds and the Earth's Radiant Energy Systems (CERES): Algorithm overview," *IEEE Trans. Geosci. Remote Sens.*, vol. 36, no. 4, pp. 1127–1141, Jul. 1998.
- [20] B. A. Wielicki, B. R. Barkstrom, E. F. Harrison, R. B. Lee, III, G. L. Smith, and J. E. Cooper, "Clouds and the Earth's Radiant Energy System (CERES): An Earth Observing System experiment," *Bull. Amer. Meteorol. Soc.*, vol. 77, no. 5, pp. 853–868, 1996.



**Cédric Bertrand** received the M.Sc. and Ph.D. degrees in applied natural sciences (environmental sciences) from the Université Catholique de Louvain (UCL), Louvain-la-Neuve, Belgium, in 1994 and 1998, respectively.

He was a Research Scientist with the Institut d'Astronomie et de Géophysique G. Lemaître, Department of Physics, UCL, from 1994 to 1999. He then joined the Centre d'Applications et de Recherches en Télédétection, Université de Sherbrooke, Sherbrooke, QC, Canada, where he held a postdoctoral position in the field of aerosol retrieval from satellite data. Since September 2001, he has been working on the Geostationary Earth Radiation Budget ground segment with the Remote Sensing from Space Section, Royal Meteorological Institute of Belgium, Brussels. His previous research interests include decadal–centennial-scale climate variability (patterns and nature of climate change and their relevance to understanding present climate change and future projections of climate change).



**Joanna Futyan** received the B.A. and M.Sci. degrees in natural sciences (physics) from Cambridge University, Cambridge, U.K., and the Ph.D. degree in atmospheric physics from Imperial College, London, U.K., in 2002 and 2005, respectively.

She is currently a Postdoctoral Research Scientist with Columbia University, New York, and the Institute for Space Sciences, New York. Her research interests include the radiative effects of tropical clouds and the evolution of tropical convective systems over their life cycle, and the development of clear-sky flux products for the Geostationary Earth radiation Budget project.



**Alessandro Ipe** received the M.S. degree in physics engineering and the M.S. degree in theoretical physics from the Université Libre de Bruxelles, Brussels, Belgium, in 1998 and 1999, respectively.

He is currently a Research Assistant with the Department of Observations, Royal Meteorological Institute of Belgium (RMIB), Brussels. He is also a Geostationary Earth Radiation Budget (GERB) Team Member and is responsible for the retrieval of cloud optical properties from the narrow-band SEVIRI imager in the RMIB GERB ground segment processing.



**Luis Gonzalez** received an engineering degree in physics from the Université Libre de Bruxelles (ULB), Brussels, Belgium, in 1992.

After one year of research at ULB on neural networks, he worked on digital signal and image processing for real-time systems. He is currently a Research Assistant with the Department of Observations, Royal Meteorological Institute of Belgium (RMIB), Brussels, where he works on the RMIB Geostationary Earth Radiation Budget ground segment processing.



**Nicolas Clerbaux** received an engineering degree in physical sciences from the Université Libre de Bruxelles, Brussels, Belgium, in 1992.

He is currently an Assistant Research Scientist with the Remote Sensing from Space Section, Royal Meteorological Institute of Belgium, Brussels. His research interests include the inversion of satellite measurements for the evaluation of the Earth radiation budget.